Annals of Biomedical Engineering (© 2023)
https://doi.org/10.1007/s10439-022-03123-8

BMES BIOMEDICAL ENGINEERING SOCIETY

Original Article

The Influence of Fluid Shear Stress on Bone and Cancer Cells Proliferation and Distribution

LAHCEN AKERKOUCH, HANEESH JASUJA, KALPANA KATTI, DINESH KATTI, and TRUNG LE

Department of Civil, Construction and Environmental Engineering, North Dakota State University, Fargo, ND, USA

(*Received 28 May 2022; accepted 25 December 2022*)

Associate Editor Stefan M. Duma oversaw the review of this article.

Abstract—We investigated the potential correlation between the fluid shear stress and the proliferation of bone prostate cancer cells on the surface of nanoclay-based scaffolds in a perfusion bioreactor. Human mesenchymal stem cells (hMSCs) were seeded on the scaffolds to initiate bone growth. After 23 days, prostate cancer cells (MDAPCa2b) were cultured on top of the osteogenically differentiated hMSCs. The scaffolds were separated into two groups subjected to two distinct conditions: (i) static (no flow); and (ii) dynamic (with flow) conditions to recapitulate bone metastasis of prostate cancer. Based on measured data, Computational Fluid Dynamics (CFD) models were constructed to determine the velocity and shear stress distributions on the scaffold surface. Our experimental results show distinct differences in the growth pattern of hMSCs and MDAPCa2b cells between the static and dynamic conditions. Our computational results further suggest that the dynamic flow leads to drastic change in cell morphology and tumorous distribution. Our work points to a strong correlation between tumor growth and local interstitial flows in bones.

Keywords—CFD, Bone metastasis, Fluid shear stress.

INTRODUCTION

bone metastasis typically occurs at the advanced stages of cancer, mainly across the axial skeleton, such as the spine and pelvic bones,[16] where it leads to severe complications in patients, such as skeletal defects, resulting in high patient mortality. While it is unclear on the precise mechanisms cancer metastasis to bone, it is hypothesized that bone facilitates suitable micro-environment for cancer cells to grow.[13]

One important factor of the bone micro-environment is the impact of fluid flow. Bancroft *et al.* demonstrated an enhanced extracellular matrix generation by osteoblast cells when the flow rate increased from 0.3 to 3 mL/min in fibre mesh titanium scaffolds.[3] On the other hand, substantial cell death was observed of MC3T3-E1 osteoblast-like cells at a flow rate of 1.0 mL/min in decellularized trabecular bone scaffolds.[5] However, the reported physiological interstitial fluid flow velocities in the bone are ranging between 0.1 and 5 μm/s.[18] Furthermore, Yourek *et al.* investigated whether fluid flow-induced shear stress affects the differentiation of bone marrow-derived human mesenchymal stem cells (hMSCs) into osteogenic cells.[18] Their results revealed an increased osteogenic differentiation of hMSCs subjected to shear stress at days 4 and 8 compared to those cultured in static conditions. Therefore, the impact of flow on hMSCs has been confirmed. However, it is unclear on the appropriate range fluid flow, which promotes the growth of hMSCs.

In addition to its impact on hMSCs, the role of fluid shear stress (FSS) was also emerged as a critical factor for tumor metastasis.[15] Recent studies have provided evidence on the link between continuous fluid flow and cancer progression.[17] In particular, the effect of FSS has been shown to impact cancer cells in many *in vitro* studies. For instance, the influence of FSS was observed in regulating endothelial barrier function and expression of angiogenic factors.[4] However, there is a gap in knowledge on how fluid forces affect the growth of cancer cells as they arrest at the extravasation site.

Address correspondence to Trung Le, Department of Civil, Construction and Environmental Engineering, North Dakota State University, Fargo, ND, USA. Electronic mail: trung.le@ndsu.edu

Published online: 02 January 2023

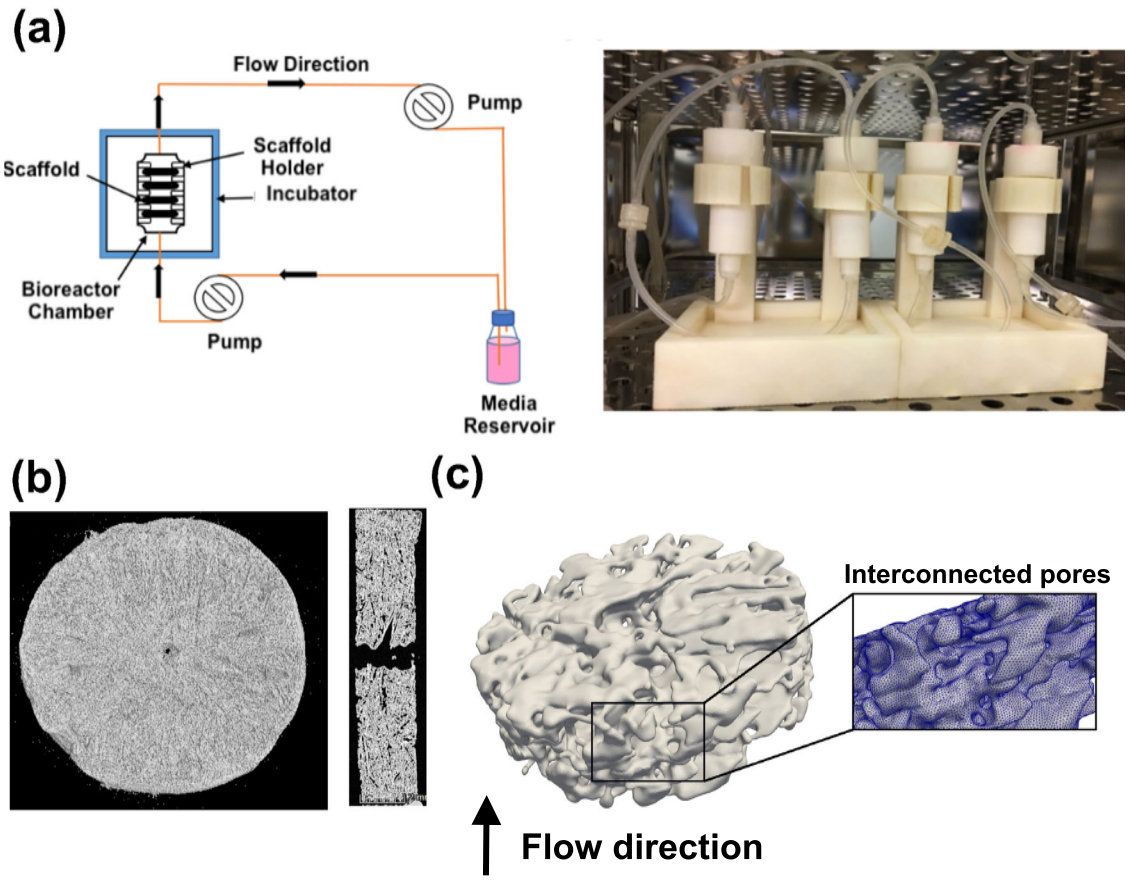

FIGURE 1. The components of the experimental apparatus. (a) The schematic diagram of the bioreactor system including the locations of four scaffolds (left). The actual bioreactors and the connected tubes (right); (b) The Micro-CT scan of one scaffold specimen showing one large hole at its center. Note that this realistic model only considers pores with a diameter larger than 70 μm due to the resolution limit of the micro-CT scan; (c) 3D geometrical reconstruction of the scaffold surface from the high-resolution micro-CT scan. The inset shows the triangular surface mesh of the interconnected pores.

As the first step to address this gap in bone, our previous work (Fig. 1a) consisted in developing a perfusion bioreactor to facilitate the co-culture of hMSCs and prostate cancer cells on nanoclay-based scaffolds under flow (dynamic) condition.[7] The polymer nanoclay-based scaffolds are highly porous structures (86.1%), with pore size ranging from 10 to 300 μm while maintaining a high compressive modulus of 2.495 MPa. It was observed that continuous fluid flow altered the orientation, and morphology of prostate cancer cells and caused a change in their gene and protein expressions. However, the precise hydrodynamic conditions at the cellular level have not been evaluated, especially in the vicinity of the scaffold pores.

Based on our previous work on cell morphologies and gene expressions,[7] we hypothesize that fluid-derived shear stress regulates the growth and proliferation of cells within the experimental scaffolds. Experimental and computational works are carried out simultaneously to probe the influence of the mechanical stresses on cancer cell growth in a full-scale nanoclay-based scaffolds positioned within a perfusion bioreactor. The objectives of our study are: (i) identify the favorable condition to grow prostate cancer cells in a dynamical culture scaffold; (ii) establish a relationship between scaffold micro-structures and internal flow characteristics; and (iii) correlate cellular morphology and FSS. The obtained results will provide guidance on controlling cell proliferation in future works.

METHODOLOGY

Experimental Protocols and Configurations

Bioreactor Design

The bioreactor chambers and their components were designed using *SolidWorks* software and fabricated using Formlabs Form-2 3D Printer as described

in detail in our previous work.[7] Briefly, the chambers were connected to the flow regulated pump and media bottles by silicone tubing (Peroxide-Cured Silicone, ID 1.42 mm, Ismatec). The flow rate was maintained at $Q = 0.2$ mL/min for all experiments. The chambers and media bottles were placed inside the incubator to maintain optimum conditions for cell survival at 37°C, 5% CO_2 and high moisture (Fig. 1a).

Preparation of the PCL/In Situ HAP Clay Scaffolds

We have developed a protocol to prepare the scaffolds, and thus only short description of the procedure is described here.[7] Briefly, sodium montmorillonite (Na-MMT) clay was modified with 5-aminovaleric acid amino acids modifiers to increase the d-spacing between clay sheets. Next, hydroxyapatite (HAP) was intercalated into the galleries of modified clay to form *in situ* HAP Clay. The scaffolds were prepared using freeze–drying method by mixing polycaprolactone (PCL) polymer and 10 wt% *in situ* HAP Clay.

Micro-CT Sample Preparation and Imaging

Scaffold samples were scanned using a micro-CT scanner (GE Phoenix vltomel xs X-ray computed tomography system) with 80 kV X-ray energy source and 350 μA current intensity with a molybdenum target. Sample magnification was carried out with a voxel size of 15.51 μm. The diameter and thickness of the scaffold were estimated as approximately 12 mm and 3 mm, respectively. The micro-CT image of the scaffold in Fig. 1b shows that the scaffold possesses interconnected pores, which are necessary for fluid flow to travel through the scaffolds.

Cell Culturing and Seeding

Human mesenchymal stem cells (hMSCs Lonza, PT-2501) were cultured in MSCGM Bullet kit medium (Lonza, PT-3001). Human prostate cancer (PCa) cells line MDAPCa2b (ATCC® CRL-2422™) were cultured in media comprised of 80% BRFF-HPC1 (AthenaES, 0403), 20% fetal bovine serum (FBS) (ATCC, 30-2020), and 1% Penicillin-Streptomycin (Gibco). The details of cell seeding steps are shown in Fig. 2. Media was changed every 2 days for static cultures and every 3 days for dynamic cultures. hMSCs and PCa media were utilized in 1:1 ratio after PCa cells seeding step. Note that both hMSC and PCa cells were seeded on the back surface of the scaffold. The rationale for this protocol will be further discussed in the experimental results section.

Cell Viability

Previously, we studied cell proliferation and their phenotype changes on scaffold surfaces for an extended period of 6 weeks and analyzed hMSCs viability for 41 days.[2,10] In brief, cell-seeded scaffolds were removed from the culture medium on Day 0, 5 and 10 then washed twice with PBS. Scaffold samples seeded with hMSCs in a 24-well plate under static conditions and incubated at 37°C, 5% CO_2 for 24 h with Day 0 considered as the Control. Next, the scaffolds were placed in a new 24-well plate with a solution containing DMEM-12 and WST-1 reagent (1:1) and incubated for 4 h in an incubator. After incubation, the intensity of yellow color was measured at 450 nm using a microplate spectrophotometer (Bio-Rad). The change in color from a slight red to yellow occurs due to the cleaving of tetrazolium salts of WST-1 reagent to formazan by metabolically active cells.

Live-Dead Assay and DAPI Staining

The viability of hMSCs was examined by live/dead staining (Biotium, 30002-T). Here, The scaffolds containing hMSCs at different time points (Day 0, Day 10, and Day 23 in Fig. 2) under both conditions were rinsed twice with warm PBS. The number of days for monitoring (e.g., 0, 10 and 23) were chosen to optimize the time frame for hMSCs osteogenic differentiation by measuring osteogenic markers such as ALP, OCN and RUNX2.[7,9] Further, the scaffolds were incubated in a solution containing 2 μM calcein AM and 4 μM Ethidium Homodimer III (EthD-III) in PBS for 30 min at room temperature for staining live cells and dead cells, respectively as per manufacturer's protocol. The scaffolds were imaged under Zeiss Axio Observer Z1 LSM 700 confocal microscope using Ex/Em wavelengths described in manufacturer's protocol.

To assess the distribution of hMSCs on the scaffold surface, all four scaffold samples were retrieved from the bioreactor chamber and cells were fixed using 4% paraformaldehyde solution. Next, the cells were counterstained with 4,6- diamidino-2-phenylindole (DAPI), and images were taken under Zeiss Axio Observer Z1 LSM 700 confocal microscope.

Histologic Examination

The samples were fixed with 4% formaldehyde, dehydrated in graded series of ethanol, and embedded in paraffin wax. Consecutive sections were cut from the paraffin blocks into 5 μm slides, sections were deparaffinized and stained with Hematoxylin and Eosin to assess cell distribution on the scaffold surface.

Scanning Electron Microscopy (SEM)

The samples containing hMSCs and sequentially cultured PCa cells were retrieved from both culturing conditions on Day 23, Day 23 (+10), and Day 23

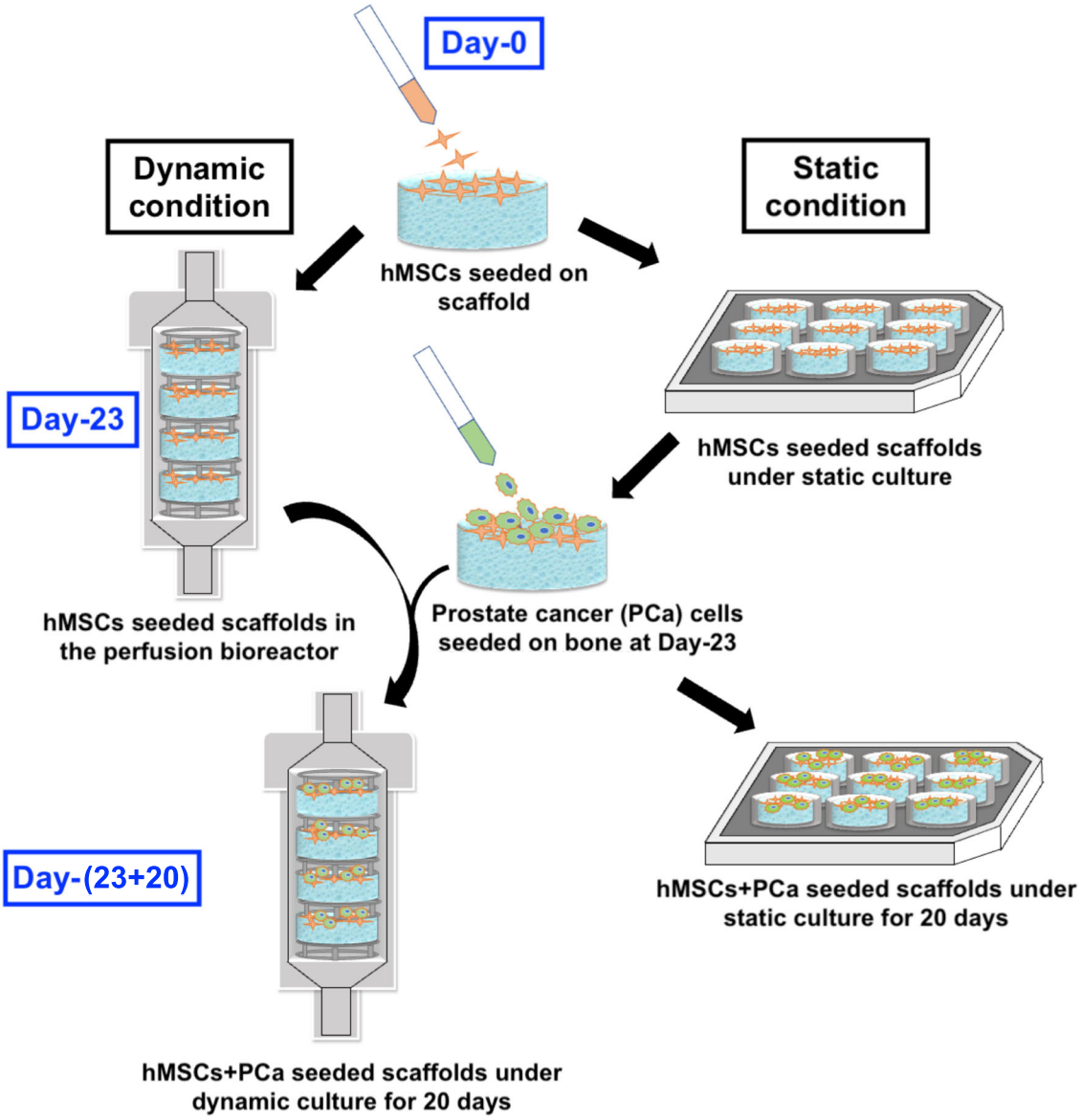

FIGURE 2. The experimental protocol for co-cultured hMSCs and prostate cancer (PCa) cells on the back surface of the scaffolds under static (right side) and dynamic (left side) conditions. 5×10^5 hMSCs cells were seeded on each scaffold in a 24-well plate and incubated at 37°C and 5% CO_2 inside the incubator for 24 h, considered as Day 0 (positive control). After 24 h, the hMSCs seeded scaffolds are separated into two groups subjected to different hydrodynamic conditions. The first half of the scaffolds remained in the incubator (static condition). The remaining half of the hMSCs seeded scaffolds were transferred into the bioreactor followed by culturing for 23 days for their osteogenic differentiation (dynamic condition). After 23 days, 1×10^5 cells of prostate cancer were seeded on bone containing scaffolds under static and dynamic conditions. Note that the scaffolds were removed from the bioreactor for cell seeding purpose. They were transferred back into their respective locations after 4 h of incubation. Prostate cancer cells seeded on bone scaffolds were cultured for 20 days under both conditions.

(+20), respectively and washed twice with PBS. Further, the cells on the scaffolds were fixed with 2.5% glutaraldehyde overnight at 4 °C. Next, the cells were dehydrated with ethanol series (30, 50, 70, 90, and 100%), and the scaffolds were dried using hexamethyldisilazane. The dried scaffolds were sputter-coated with gold and mounted on SEM stubs for scanning under the scanning electron microscope (JEOL JSM-6490LV).

Numerical Simulation

Bioreactor Geometrical Model

From the bioreactor design (Fig. 1), the computational models are reconstructed as seen in Fig. 3 with the exact dimensions. The *SolidWorks* model of the bioreactor was converted to the STereoLithography (STL) format, and re-meshed as an unstructured mesh.

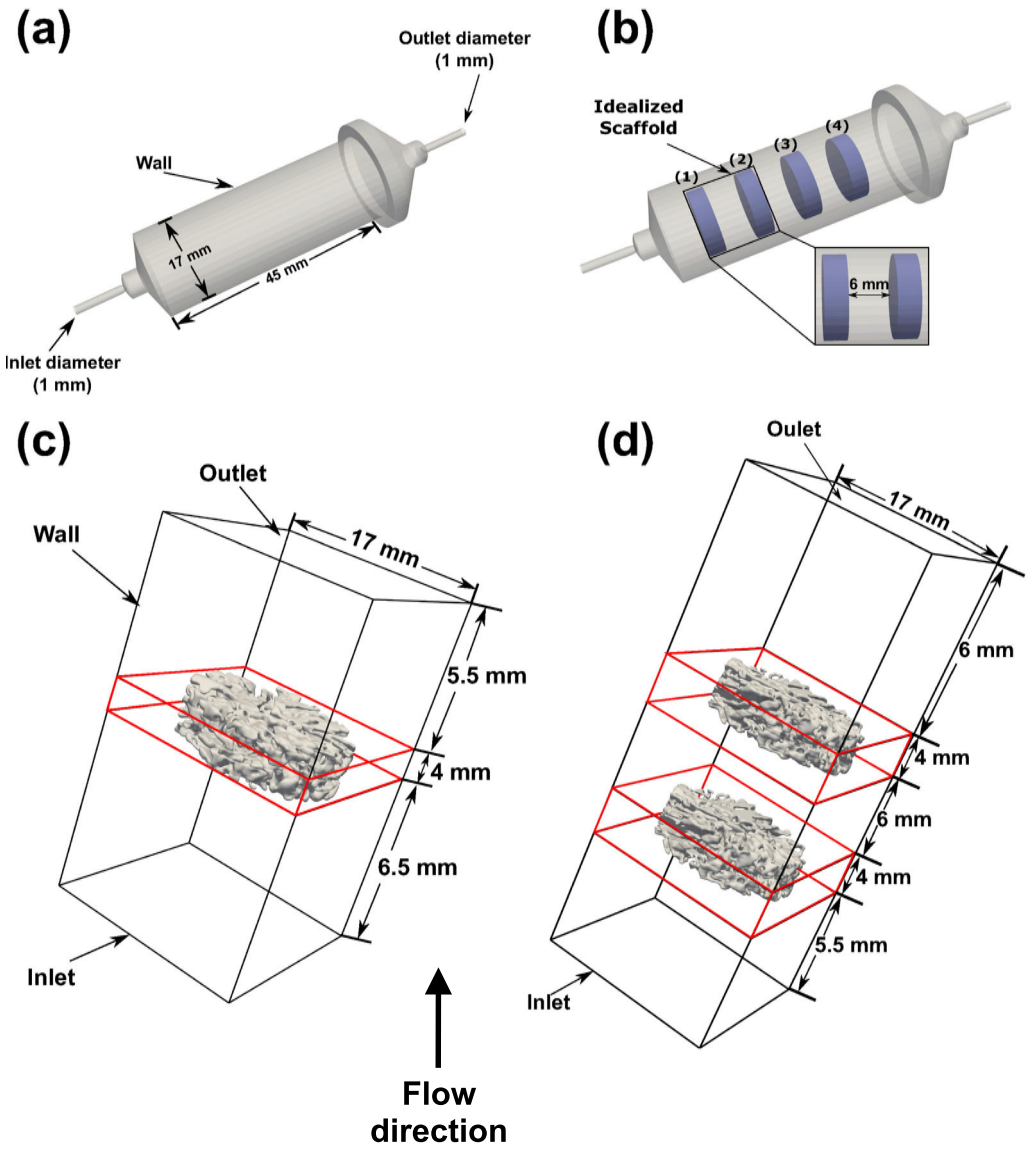

FIGURE 3. Computational configurations for four cases: A, B, C, and D (see Table 2). (a) Fluid flow in an empty bioreactor (Case A). The bioreactor's inlet and outlet are circular tubes with diameters of 1 mm, and the diameter and length of the bioreactor chamber are 17 mm and 45 mm, respectively; and (b) The impact of four idealized scaffolds on the flow structure of the bioreactor (Case B). The locations of the idealized scaffolds are in the exact arrangement as in the experimental settings. The first scaffold locates at a distance of 6 mm from the bioreactor inlet, and each two consecutive scaffolds are separated with 6 mm from each other. The diameter and thickness of this model are 12 mm and 3 mm, respectively. In Case C and D, the 3D geometrical model of the scaffolds from the micro-CT scan are used to compute fluid flow in pores; (c) Flow through the pores of one scaffold (Case C); (d) The impact of the second (downstream) scaffold on flow structures inside the first scaffold (Case D). The computational domains are defined as a rectangular box with similar dimensions to the bioreactor chamber, and discretized using structured blocks as shown in Table 2. The red box indicates the area where the computational grid points are concentrated (around 40 millions points) to resolve individual pores. The computational domain includes two buffer regions near the inlet and outlet to ensure a realistic flow field surrounding the scaffolds. Flow is from the bottom to the top (black arrow).

At the inlet, a uniform flow velocity of 4.24 mm/s is applied for all cases.

Scaffold Geometry

There is a large disparity of fluid flow scale within the bioreactor across several orders of magnitudes. The flow structures varies from milimeter scale (bioreactor inlet) to micrometers (scaffold pores). It is challenging to resolve all the flow features in the bioreactor with the existing computational resources. Therefore, a multi-scale approach is carried out to resolve the flow structures systematically.

Here, we consider two types of scaffolds to provide the estimations of millimeter and micrometer scale flow

TABLE 1. The details of surface meshes (triangular elements) for the bioreactor and the scaffolds (Fig. 1) in numerical simulations (Fig. 3).

Surface mesh	Vertices	Elements
Bioreactor	3759	7518
Idealized scaffold	430	860
Micro-CT scaffold	276, 913	555, 086

The surface meshes of the bioreactor and the idealized scaffold are generated from the geometric models using the commercial software Gridgen. The idealized scaffolds (Fig. 3b) are considered as impervious cylinders. The geometry of the micro-CT scaffold is illustrated in Fig. 1.

patterns. First, an idealized model of the scaffolds is considered as an impervious cylindrical body (Fig. 3b). This idealized model is used to provide a general (large-scale) pattern of the flow inside the bioreactor and the surrounding areas of scaffolds. Second, the realistic scaffold model is re-constructed from the micro-CT data (Fig. 1b). The cross-section view in Fig. 1b highlights the highly interconnected pores, which are necessary for the interior fluid flows. The open-source software *Slicer3D* is used to generate the full-scale 3D surface mesh of the scaffold. The STL model of the scaffold was smoothed and re-surfaced using the open-source software *Meshmixer* (Fig. 1c). The details of the two types of scaffolds are explained in Table 1.

Numerical Methods

The DMEM fluid was considered to be an incompressible Newtonian fluid with constant density ($\rho = 1000$ kg/m^3 and kinematic viscosity ($\nu = 0.78 \times 10^{-6}$ m^2/s).[7] The numerical method employed in this work has been extensively described and thoroughly validated against *in vitro* and *in vivo* data for millimeter to micrometer scales.[11] Therefore, only a brief description of the numerical method is presented in this section. For more details about the method, the reader is referred to our previous publications.[1] The governing equations for the fluid are modeled as three-dimensional Navier–Stokes equations. The governing equations are solved using the sharp-interface curvilinear-immersed boundary (CURVIB) method in a background curvilinear domain that contains the complex geometries of the bioreactor and scaffold models. The discrete equations are integrated in time using a fractional step method. A Newton–Krylov solver is used to solve the momentum equations in the momentum step, and a Generalized Minimal Residual (GMRES) solver with multigrid preconditioner is employed for the Poisson equation.

Computational Setups

A multi-scale approach to investigate the flow around the scaffold was carried out. First, the flow around the scaffolds was examined in large-scale patterns (millimetre scale) to understand the impacts of the scaffolds arrangement on the FSS distribution. Second, the overall distribution of FSS on each scaffold was examined to investigate the blocking effect of consecutive scaffolds. Finally, the internal flow inside each scaffold is studied via a series of high-fidelity simulations to resolve individual pores in four computational setups as discussed below.

First, the large-scale model is simulated using the entire bioreactor chamber (Case A) without any scaffolds. The 3D surface mesh of the empty bioreactor is illustrated in Fig. 3a. The details of the bioreactor mesh are shown in Table 1. The simulation setup is used to investigate the large-scale flow patterns inside the bioreactor in the absence of the scaffolds.

Second, the role of the scaffolds in changing the large-scale flow pattern within the bioreactor is examined. Four idealized scaffolds were placed within the bioreactor as shown in Fig. 3b, their details are shown in Table 1. Due to the idealized geometry, no pores are considered in this computational configuration. Two specific surfaces of the idealized scaffolds are of interest: (i) the front, and (ii) the back surfaces. The front and back surfaces denotes the upstream and downstream sides of the scaffold (Fig. 1c). The role of these surfaces is discussed further in the simulation results section.

Third, the flow pattern inside the scaffold's pores is examined in Case C (Fig. 3c). To capture accurately the intricate porous geometry, the micro-CT scaffold model is represented with highly dense unstructured mesh as depicted in Fig. 1c and Table 1. Due to this complexity of the scaffold's porosity architecture, a high number of grid points in the computational domain is needed to resolve the flow and FSS at the level of the pores as shown in Table 2.

Fourth, Case D is used to investigate the impacts of the blocking effect by the scaffolds on the local FSS at the entire surface volume of the scaffold. Two full-scale scaffolds were placed inside the computational domain following the same experimental arrangement in Fig. 3d and Table 2.

In all four cases, an inlet uniform velocity profile was applied. The Neumann boundary condition was specified for all velocity components at the outlet. No-slip and no-flux conditions are prescribed at all boundary walls, which are considered rigid. In subsequent sections, the steady state solutions of the simulations are reported for the flow and FSS patterns.

RESULTS

The Dependence of hMSCs Growth on Hydrodynamic Conditions

The measured absorbance in Fig. 5 showed that the viability of hMSCs increased on Day 10 when the homeostatic condition was attained (no flows). At first, the absorbance showed a slight increase in cell proliferation from Day 0 (control) to Day 5. However, a significant increase $(*p < 0.05)$ of cell viability was observed from Day 5 to Day 10 as shown in Fig. 4b. Therefore, the static condition promotes the culturing of hMSCs.

Under dynamic condition, the hMSCs proliferation was observed to increase significantly from Day 0 to Day 10 when they were under continuous flow rate of $Q = 0.2$ mL/min (dynamic condition). Due to the difference in hydrodynamic conditions, the scaffolds have two distinct surfaces: (i) front; and (ii) back surfaces under dynamic condition. The front surface faces the flow direction while the back surface locates at the downstream side of the scaffold. The difference in hydrodynamic conditions produced distinct trends in cell proliferation. As evident in Fig. 4a, seeding the hMSCs on the front surface of scaffolds led to a major cell death at Day 10. In particular, the viability of hMSCs decreased significantly $(**p < 0.01)$ from Day 0 to Day 10. On the contrary, in Fig. 4b the hMSCs showed a clear preference in proliferating on the back surface. Because the hMSCs did not proliferate on the front surface, they were seeded only on the back surface of the scaffold in subsequent experiments within the perfusion bioreactor (Figs. 5a, 5b). Under dynamic condition, a significant increase in cell proliferation and morphological change were observed. There existed non-uniform presence of DAPI stained hMSCs nuclei in all four scaffolds at Day 23 as seen in Fig. 5b. Furthermore, the hMSCs were observed to be stretched in a well-defined direction under the impact of fluid forces as seen in Figs. 5c and 5d as opposed to the random distribution of hMSCs under static condition on the Day 23. Based on the qualitative assessment of the cell viability by live-dead staining assay shown in Fig. 5c, almost all the hMSCs were observed alive along the period of 23 days. In addition, the hMSCs gained a directional orientation even early on Day 10 under dynamic condition as shown in Fig. 5c. On Day 23, SEM analysis of hMSCs under dynamic and static culturing are shown in Figs. 5e and 5f. Under dynamic condition (Fig. 5f), the cells aligned to well-defined orientation, whereas under static condition they exhibited cell aggregation (Fig. 5e). In brief, the presence of a dynamic condition altered the large scale

TABLE 2. Computational grids for numerical simulation of flows in the bioreactor: (a) Case A (the empty bioreactor); (b) Case B (the idealized scaffolds); (c) Case C (the micro-CT scaffold); (d) Case D (two full-scale scaffolds).

Case	$i \times j \times k$	$\Delta x \times \Delta y \times \Delta z$ (μm)	Total Grid Points
A	$351 \times 351 \times 351$	$100 \times 80 \times 240$	43, 243, 551
B	$351 \times 351 \times 351$	$100 \times 80 \times 240$	43, 243, 551
C	$401 \times 401 \times 491$	$20 \times 20 \times 8$	64, 481, 201
D	$401 \times 401 \times 537$	$20 \times 20 \times 16$	86, 350, 137

The computational grid is a structured mesh of size $i \times j \times k$. The spatial grid resolution in the x, y, and z direction are Δx, Δy, and Δz, respectively.

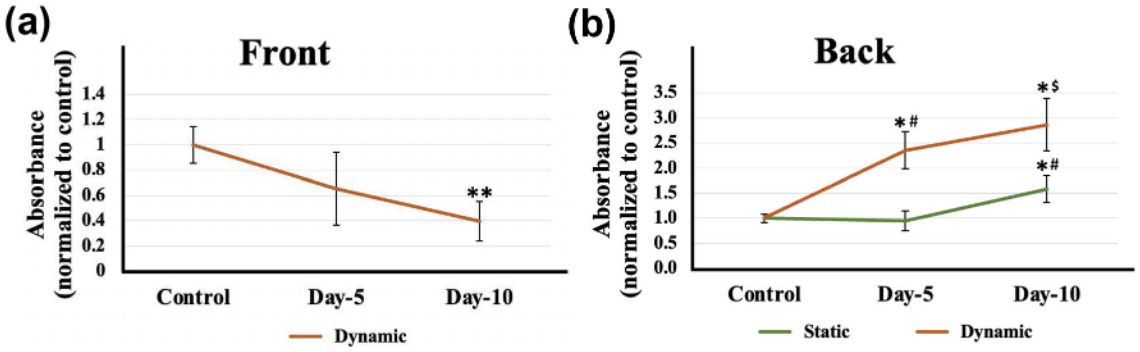

FIGURE 4. The viability and proliferation of hMSCs assessed by WST-1 viability assay under static and dynamic culture. Here, The symbol $*$ indicates statistical significance compared to the control, and the symbols $(\#, \$)$ show the statistical significance between different static and dynamic cells on specific days. (a) Evaluated metabolic activity of hMSCs seeded on scaffold's front under dynamic culture by measuring the absorbance of color at 450 nm on Day 0 (Control), Day 5, and Day 10. $**p<0.01$ indicates a significant difference between the Control and Day 10 dynamic samples; (b) Evaluated metabolic activity of hMSCs seeded on scaffold's back under dynamic culture and compared results with samples cultured under static conditions by measuring the absorbance of color at 450 nm on Day 0 (Control), Day 5, and Day 10. $*p<0.05$ indicates a significant difference between Control and Day 5 samples and between Control and Day 10 samples. $^{\#}p<0.05$ indicates a significant difference between Day 5 static and Day 5 dynamic samples and between Day 5 static samples and Day 10 static samples. $^{\$}$ $p<0.05$ indicates a significant difference between Day 10 static and Day 10 dynamic samples. Error bars indicate standard deviation (SD).

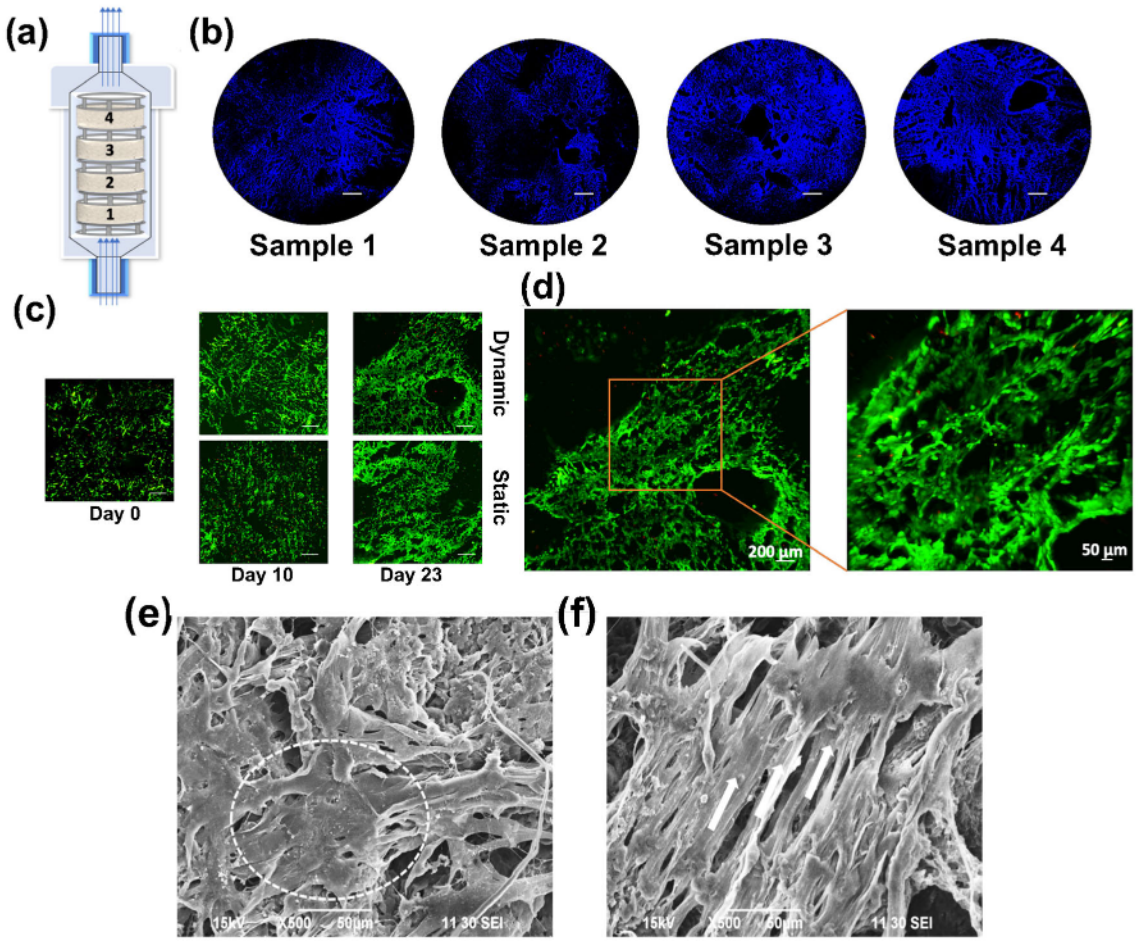

FIGURE 5. The distribution, viability and orientation of the hMSCs were investigated by nuclei DAPI staining (blue color), live-dead essay (green color), and SEM analysis. (a) Schematic showing flow direction of media through bioreactor accommodate with four scaffold samples. (b) DAPI Stained human mesenchymal stem cells (hMSCs) nucleus representing distribution of cells on the back side of the nanoclay-based scaffold grown under dynamic conditions on Day 23 (scale 1 mm). The cells are shown to posses high growth rate at the boundaries of the pores. (c) Live dead assay represents viability of hMSCs over 23 days under static and dynamic conditions, Scale 400 μm. (d) partial close-up view of hMSCs grown on scaffold on Day 23. (e) SEM data represents the random distribution of hMSCs under static culture on Day 23. (f) SEM data represents the directional alignment of hMSCs under dynamic culture on Day 23.

distribution of cells as well as the local cellular morphology.

Morphological Changes of Co-cultured hMSCs/MDAPCa2b Cells Under Continuous Flow

After culturing (static and dynamic) the seeded hMSCs for a period of 23 days for osteogenic differentiation and mineralized bone formation, prostate cancer cells (MDAPCa2b) were seeded on the top of the osteogenically differentiated hMSCs for a period of 20 days (Day 23 (+20)). Hematoxylin and eosin staining were employed to visualize the distribution of the co-cultured hMSCs + MDAPCa2b on the surface of the scaffolds on Day 23 (+20) under static and dynamic conditions as seen in Fig. 6. The morphological changes in prostate cancer cells and their distribution within scaffold under static and dynamics culturing were evaluated utilizing the SEM technique as well. To reflect the morphological changes under fluid flow, the results were both reported of the co-cultured cells on Day 23 (+10) and Day 23 (+20).

The results revealed a clear impact of the flow on the co-cultured hMSCs/MDAPCa2b growth. Under static condition the staining of hMSCs + MDAPCa2b showed that the cells nuclei were randomly distributed on the scaffold surface as seen in Figs. 6a and 6b. However, a striking feature of cellular distribution was found on the edges of the pores under dynamic condition as shown in Figs. 6c and 6d. Cell proliferation was found mostly to occur in the vicinity of scaffold's pores.

The local impact of the flow on the MDAPCa2b's morphology is further shown in Fig. 7. Under static

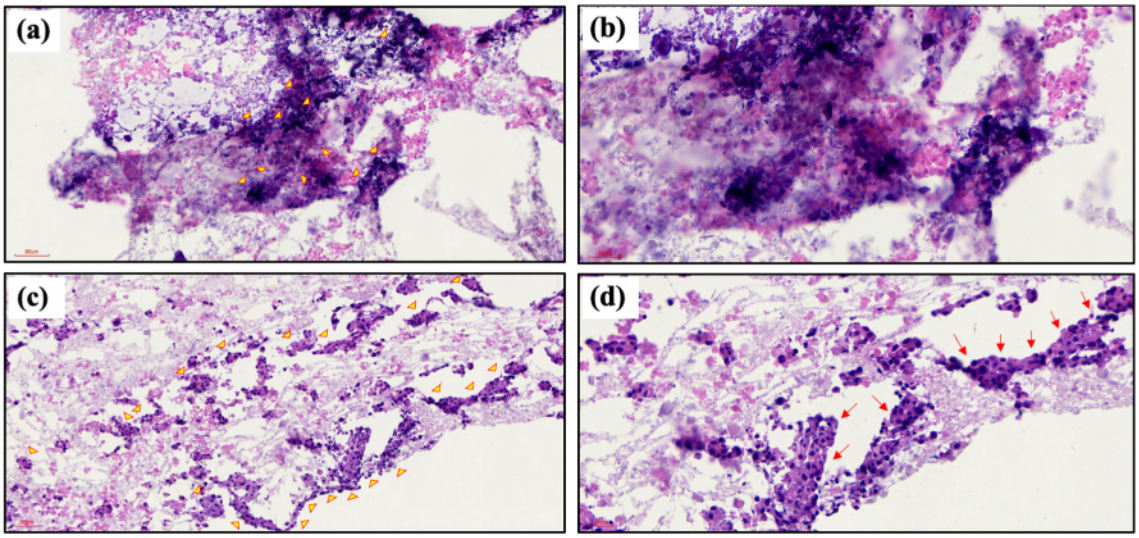

FIGURE 6. Images showing hematoxylin and eosin staining of hMSCs + MDAPCa2b sequential culture on Day 23 (+20) represent variation in cells distribution under (a, b) static culture and (c, d) dynamic culture at different scales. Here, we used an 80 mm scale bar for Figures (a, c), and a 40 mm scale bar for Figures (b, d). Figures (b, d) are enlarged views of Figures (a, c), respectively. Yellow arrows and red arrows indicate the location of tumor cells within the scaffold and around the scaffold pores, respectively.

condition, the MDAPCa2b cells were observed to form tumors with round (spherical) morphology on Day 23 (+10). The cells maintained such morphology till Day 23 (+20) with an increased in tumor size as seen in Figs. 7a and 7c. On the contrary, MDAPCa2b prostate cancer cells appeared to undergo a significant morphology change on Day 23 (+10) under dynamic culture. Their morphology was observed to consistently change over time, and appeared to form compact structures with no distinct boundaries on Day 23 (+20) as shown in Figs. 7b and 7d. Interestingly, the MDAPCa2b cells were shown to grow surrounding the pores of scaffolds under dynamic conditions in agreement with their large-scale distribution shown in Figs. 6c and 6d. Hence, our results showed a clear impact of continuous flow on the growth of co-cultured hMSCs/MDAPCa2b cells, especially around the pores as shown in Figs. 7e and 7f.

Large-Scale Flow Patterns

In case A, the flow velocity distribution within the empty perfusion bioreactor was shown in Fig. 8a. Due to the low applied Reynolds number, the flow within the bioreactor resembled closely to a Poiseuille flow profile except areas at the inlet and outlet. In particular, at the center of the bioreactor, the velocity magnitude was observed significantly lower (~ 50 μm/s). The bioreactor design provided a consistent flow condition along the chamber axis.

In case B, four idealized scaffolds were placed within the bioreactor to investigate their influence on the local flow pattern and the direction of the FSS on the surface of the scaffolds, as depicted in Figs. 8b and 8c. The presence of the idealized scaffolds altered significantly the overall distribution of the laminar fluid flow within the bioreactor as compared to Case A. Moreover, the flow velocity between the scaffold edge and the bioreactor chamber wall increased significantly up to 100 μm/s. In addition, a blocking effect was observed at the gaps between the scaffolds where the velocity magnitude was very low (up to 20 μm/s). This blocking effect was even more evident as it influenced the orientation of the FSS on the surface of the idealized scaffolds. On the first scaffold, the FSS diverged immediately toward the edge after the flow impacted the scaffold front surface. The FSS pattern converged toward the center of the back surface following the flow direction. Under the presence of the second scaffold, a flow circulation was created inside the space between the first and the second scaffolds. Therefore, the FSS on the back of the first scaffold converged to a circulation zone as evident by a separation line near the back surface center. In this circulation zone, the FSS magnitude was observed to be less than 20 μPa. This circulation pattern appeared on the back surface of the second and third scaffolds as well. On the back surface of the fourth scaffold, the FSS pattern converged back to center of scaffold's back surface since there was no blocking effect.

Flow in the Vicinity of Pores

In case C, the velocity and shear stress distributions were examined at the level of the pore resolution (Fig. 3c). Overall, the FSS distribution on the scaffold

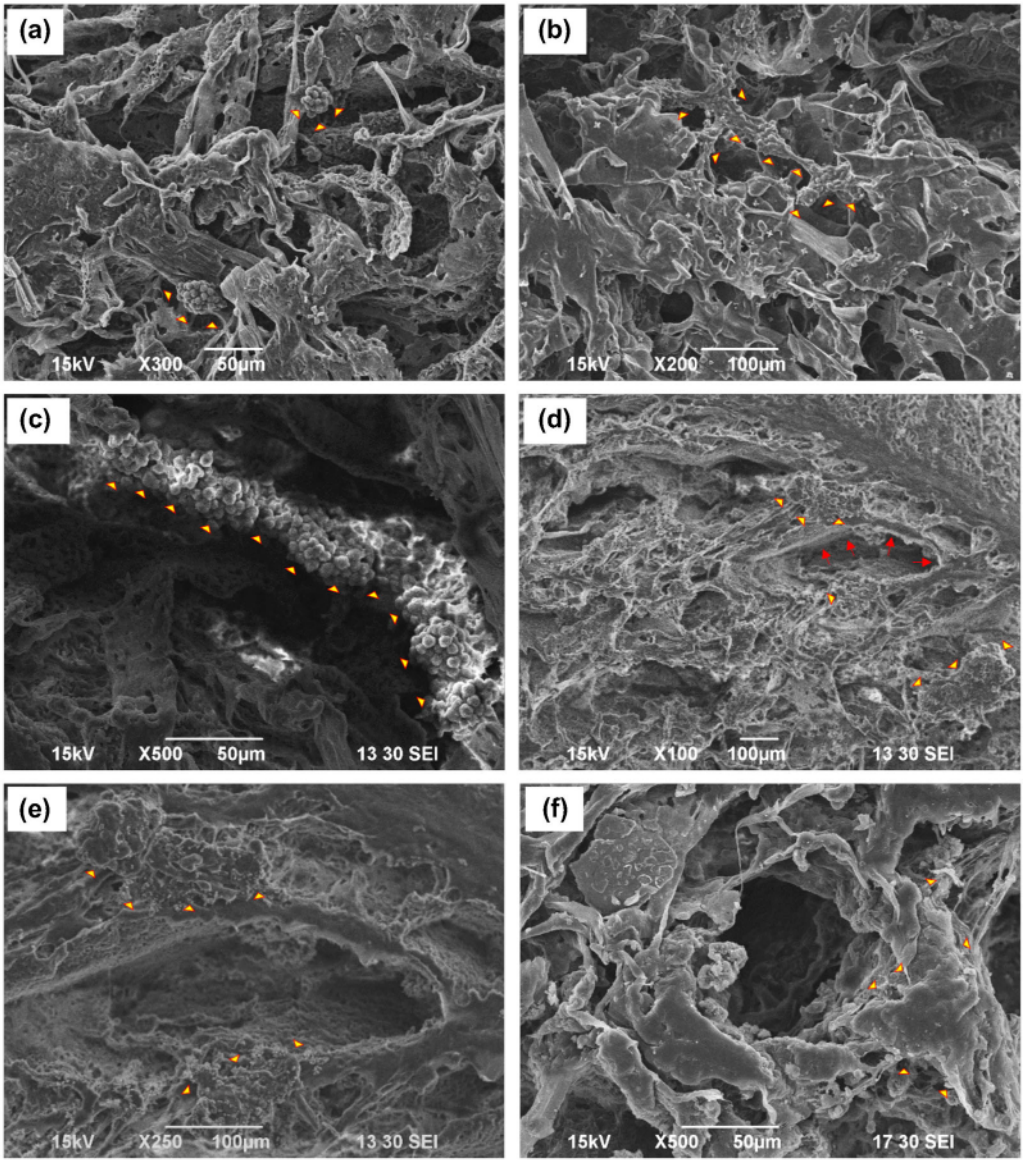

FIGURE 7. SEM data of hMSCs + MDAPCa2b sequential culture on Day 23 (+10) (a and b) and Day 23 (+20) (c and d) represents morphological variations of prostate cancer cells under (a, c) static culture and (b, d) dynamic culture. Yellow arrows and red arrows indicate the location of tumor cells and scaffold pores, respectively in the micrograph. (e) SEM data of hMSCs + MDAPCa2b sequential culture on Day 23 (+20) indicating growth of tumor cells around the scaffold pores under dynamic conditions. Yellow arrows indicate the location of tumor cells around scaffold pores, in the micrograph. (f) the close-up view of tumor cell growth around one pore.

front and back surfaces (Figs. 9a, 9b) revealed that the FSS exhibited a heterogeneous distribution on the surfaces depending on the presence of the pore geometries. The FSS contour revealed that the majority of FSS on both surfaces of the scaffold fell into the interval [0–15] μPa. The maximum FSS magnitude (greater than 50 μPa) occurred at the boundaries of the scaffold due to the narrow space between the edge of the scaffold and the domain wall. In addition, there was a large hole in the center of the scaffold leading to a flow convergence region near the hole. To illustrate the orientation of the FSS, the FSS vectors on the front and back surfaces of the scaffold were plotted in Figs. 9c and 9d. The results showed that the direction of FSS vectors followed closely the geometry of the scaffold pores. On the front surface, FSS vectors diverged toward the edges of the scaffold, except the area close to the central hole. On the back surface, the FSS pattern was more complex. The overall pattern consisted of convergence zones sur-

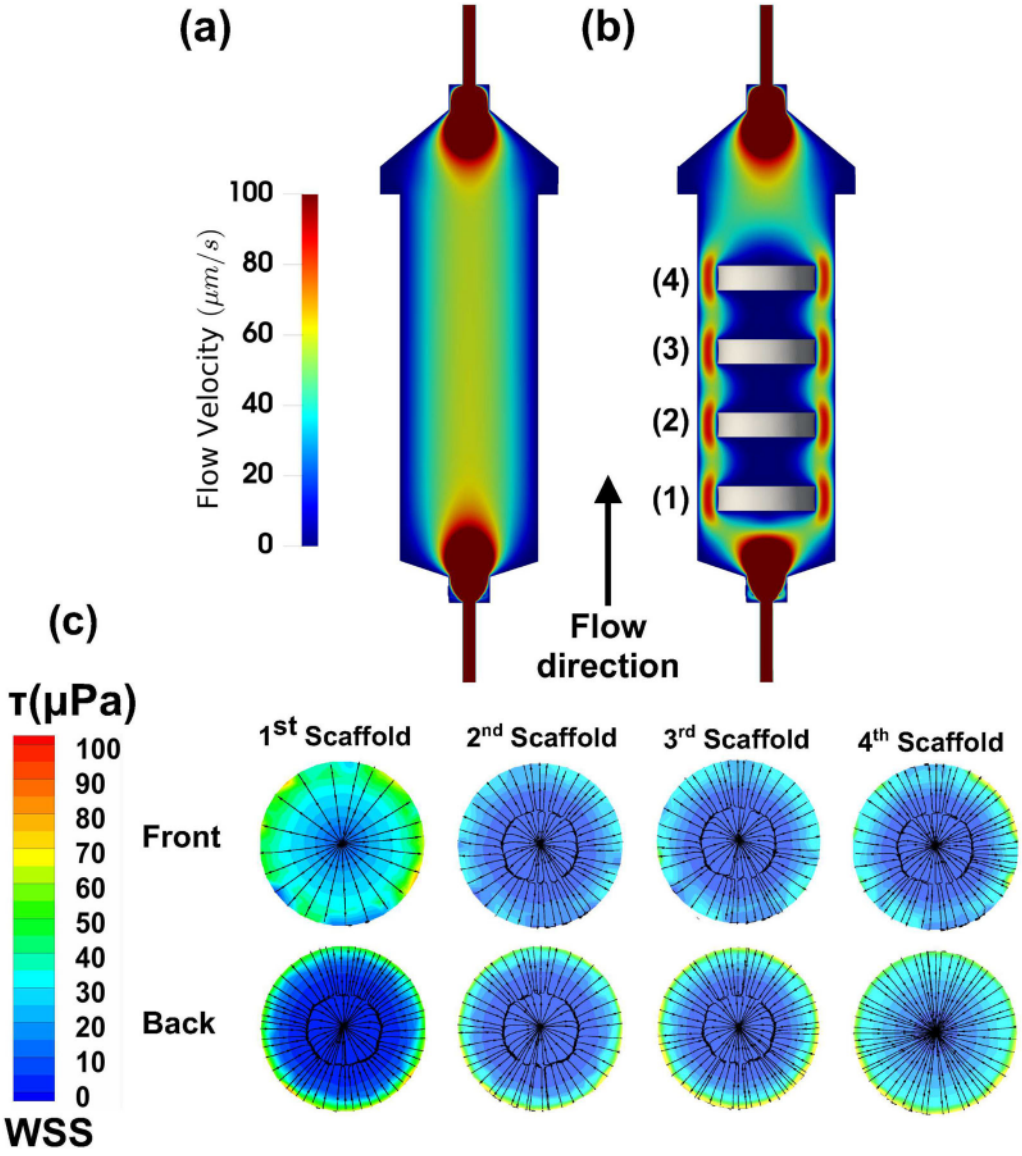

FIGURE 8. Flow velocity distribution inside the bioreactor: (a) Case A (an empty bioreactor); and (b) Case B (four idealized scaffolds). The velocity contours are plotted on the plane of symmetry of the bioreactor. The flow velocity was observed to remain low around 50 μm/s inside the bioreactor chambers. With the presence of idealized scaffolds, the flow velocity distribution is varied with the magnitude up to 20 μm/s. The Flow-induced Shear Stress (FSS) direction on the surface of the four idealized scaffolds are shown in (c). Each column represent the front and back of the idealized scaffold. The influence of the gap between two consecutive scaffolds can be observed by creating a FSS convergence zone on the surface with a magnitude between 0 and 15 μPa.

rounding the pores as shown in Fig. 9d. In brief, there was a clear distinction of the FSS characteristics between the front and back surfaces of the scaffold.

To further analyze the difference between the hydrodynamic conditions on the scaffold's front and back surfaces, the histograms of the flow velocity and FSS were plotted for layers close to the surfaces (0.8 mm thickness) in Figs. 9e and 9f. Our results demonstrated that there was a significant difference on the approaching flow velocity distribution between the front and the back surfaces as shown in Fig. 9e. Our results revealed that the fluid flow velocities on the front surface of the scaffold were observed to distribute evenly across all magnitudes up to 10 μm/s. On the contrary, the fluid flow velocity on the back surface was observed to fall almost exclusively (85%) in the interval of [0–0.5] μm/s. Despite the difference in the flow velocities between the front and back surfaces, the FSS histograms in Fig. 9f showed a consistent distribution pattern.

In order to verify the hydrodynamic conditions inside the scaffold, three horizontal planes, which are in

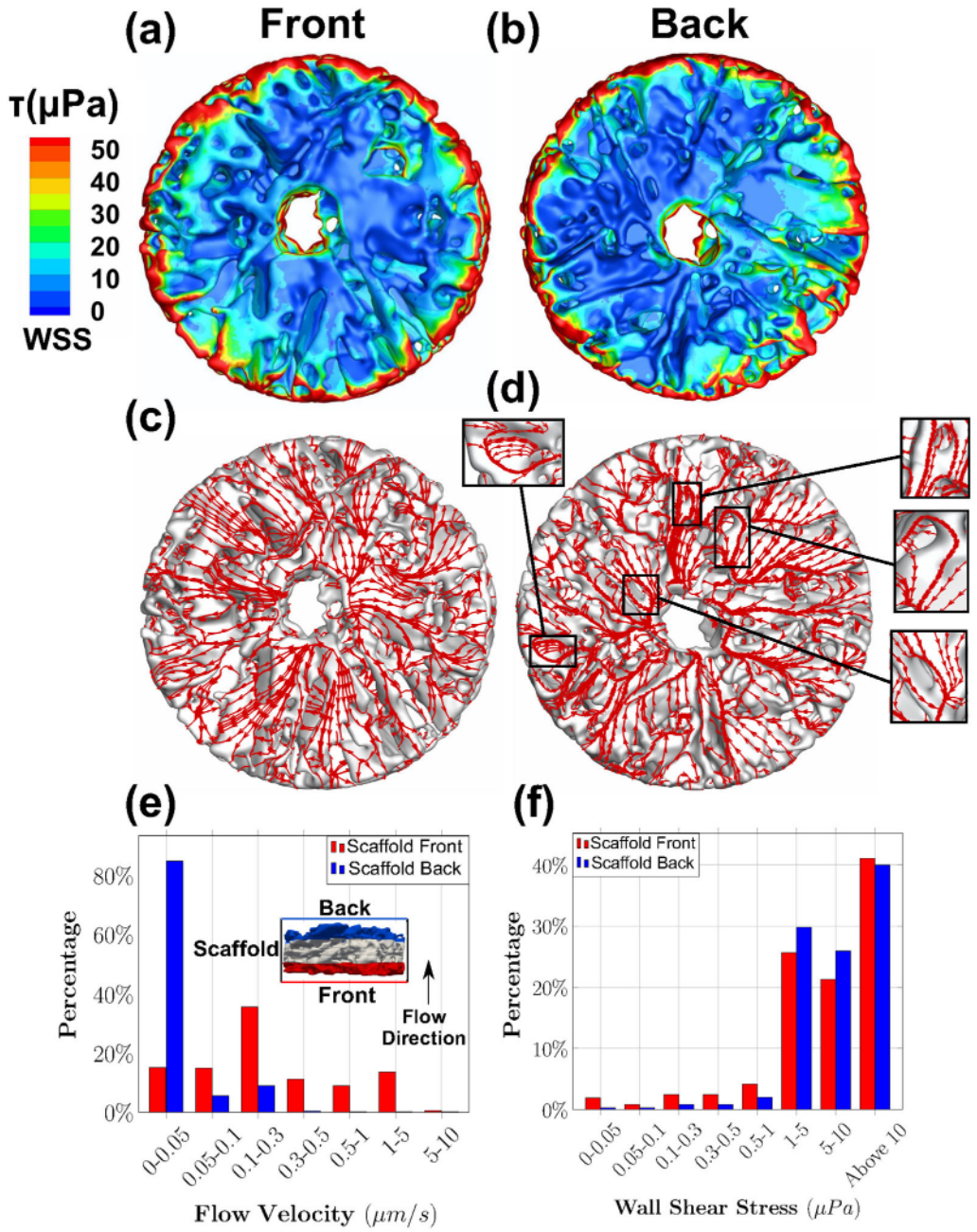

FIGURE 9. The distribution of Fluid-induced Shear Stress (FSS) on the front (a), and back (b) surfaces of one scaffold (Case C). The direction of the FSS indicated a convergence pattern surrounding the pores on the front (c), and back (d) surfaces. The insets illustrated the convergence of FSS vectors around the pores. The histograms of flow velocity and FSS in the vicinity of the scaffold's front and back surfaces were shown in (e) and (f), respectively. The vicinity region was defined as a layer of 0.8 mm thickness from the corresponding surface as shown in the inset of (e).

the position of 25, 50, and 75% thickness, were used as shown in Fig. 10. It is evident in Fig. 10a that flow the velocity was largely dependent on the pore architecture. The presence of the central hole induced a high velocity region (greater than 2 μm/s) in the scaffold's center. In addition, the complex geometry of the pores guided local high velocity regions inside the scaffold with the existence of high velocity patches. To quantify the similarity in flow and FSS distribution on these planes, the frequency histograms in Figs. 10c and 10d were used to compare the hydrodynamic conditions among these planes. Despite the geometrical irregularity, the horizontal plane cuts in Fig. 10b revealed a similar frequency distribution of FSS among the three

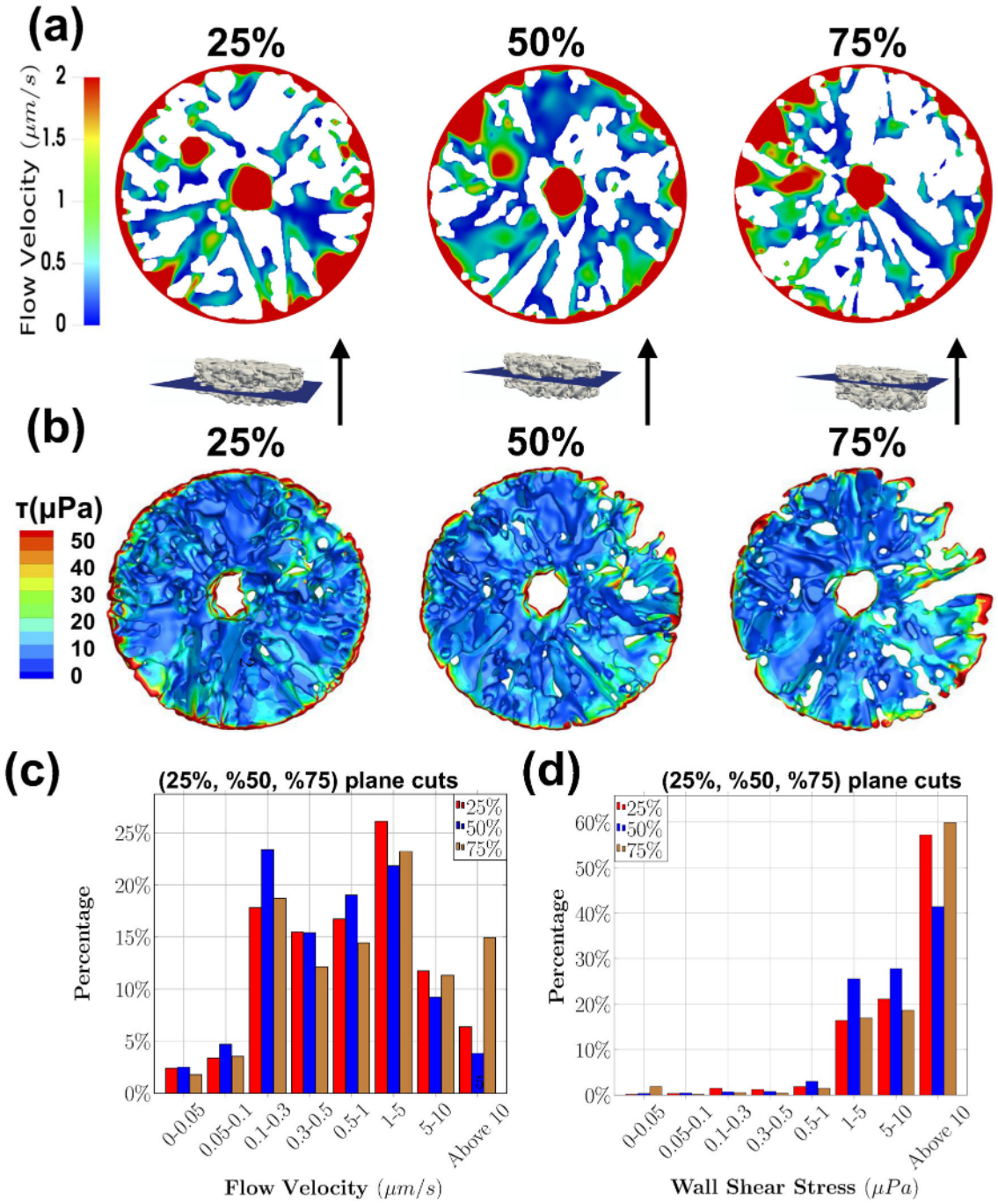

FIGURE 10. The hydrodynamic condition inside the scaffold at pore resolution (case C). The interior flow (a) velocity magnitude and (b) Fluid-induced Shear Stresses (FSS) within the scaffold were visualized from the transverse plane cuts at 25, 50, and 75% of the scaffold thickness (the horizontal inset). The flow velocities and FSS were heterogeneously distributed in each cross-sectional plane depending on the pore geometry. However, the frequency histograms demonstrated that the (c) velocity and (d) FSS distribution exhibited a similar pattern along the longitudinal (flow) direction. The majority of the flow velocities were within the interval [0.1−5] μm/s, whereas the FSS was greater than 1 μPa.

horizontal planes. The FSS value was mostly less than 10 μPa in all planes. The majority of the fluid flow velocities were within the interval of 0.1 to 5 μm/s inside the scaffold as shown in Fig. 10c, in which the range of the FSS magnitude was mostly between 1 and 10 μPa. Our results thus depicted that the overall distribution of flow velocity remained rather consistent across all three planes.

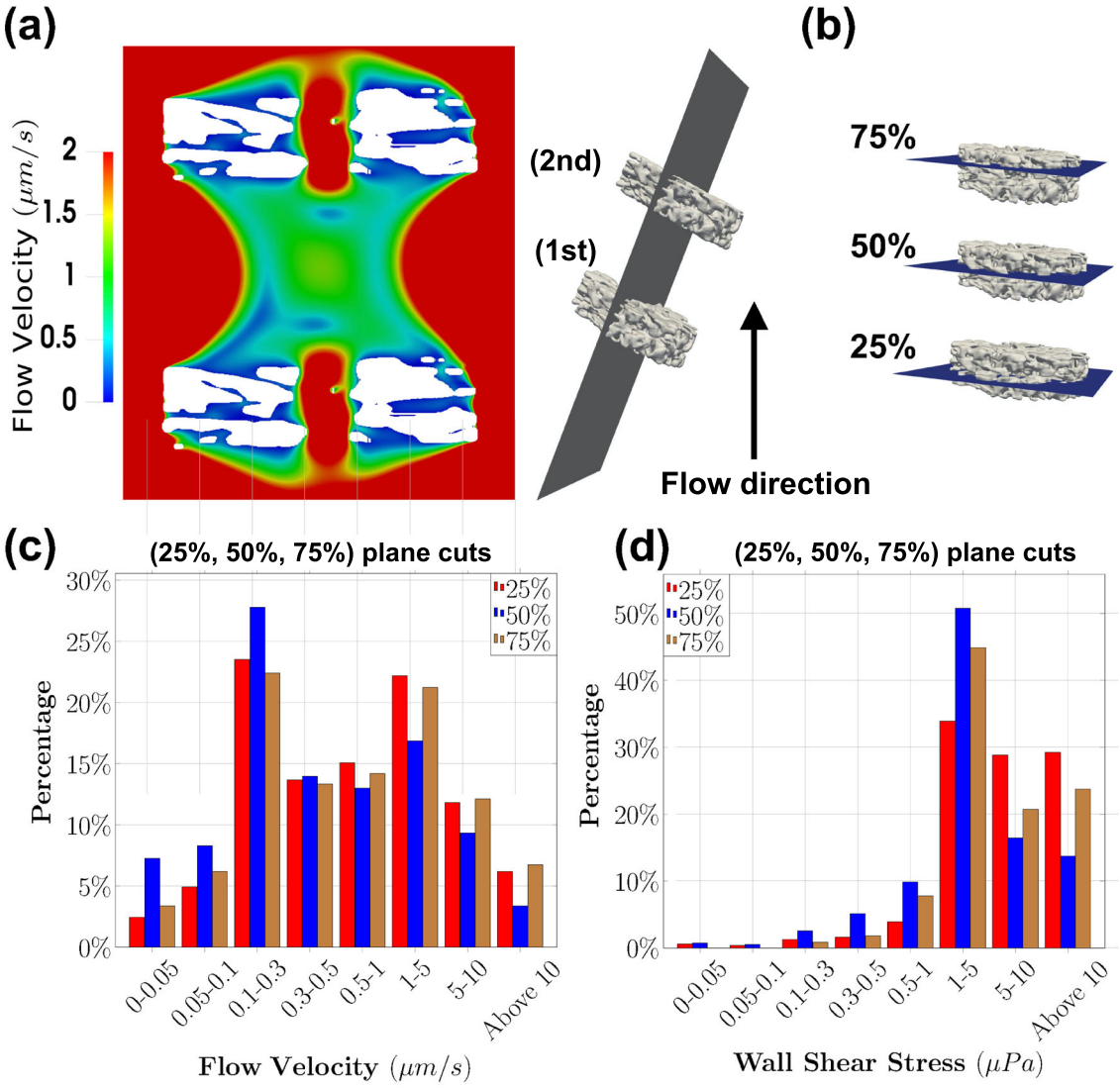

FIGURE 11. The hydrodynamic impacts of the second scaffold (case D): (a) Flow velocity contour of the two full-scale scaffolds visualized form the plane of symmetry; (b) The exact location of the 25, 50 and 75% planes inside the first scaffold; (c–d) Frequency histogram of the interior flow velocities and FSS of the first scaffold taken from the horizontal plane cuts in (b). The flow velocities and FSS within the first scaffold were observed to follow a similar trend as in the single scaffold (case C) in Fig. 10.

The Hydrodynamic Impact of Scaffold Arrangement

The scaffold arrangement has a minimal impact on the approaching velocity and shear stress distribution of the first scaffold. As shown in Fig. 11a, the velocity field between two consecutive scaffolds was observed complex. The second scaffold creates a blocking effect by inducing a reduction of flow velocity (less than 2 μm/s) in the gap between these scaffolds. This reduction creates a flow circulation zone, which covered almost entirely the gap. To examine the effect of this gap, the flow velocity and FSS at different cross-sections (25, 50, 75% in Fig. 11b) of the first scaffold are computed. Their histograms showed consistent patterns of hydrodynamics at all cross-sections as shown in Figs. 11c and 11d. The majority of the flow velocities were within the range of [0.1−5] μm/s, while most of the FSSs occurred from 1 μPa and above as seen in Figs. 11c and 11d. Comparing with the histograms in Figs. 10 and 11, it is evident that the impact of the second scaffold is insignificant.

DISCUSSION

Previously, our dynamic culturing results has been shown to accelerate the hMSCs proliferation and differentiation, in which the FSS induced by interstitial flow is considered a key parameter in activating, and maintaining the proliferation and differentiation of

hMSCs for bone growth.[7] Our group also examined the effect of nanoclay on osteogenic differentiation of hMSCs by comparing MSCs differentiation on scaffolds with or without nanoclays, showing that the mineralized ECM was formed by MSCs without use of osteogenic supplements.[8] In addition, we observed that the presence of MSCs significantly influenced tumour morphology, and gene expressions under static conditions.[12,13] Furthermore, different morphological changes and osteogenic rates were observed in static vs. dynamic conditions, in which dynamic culturing was characterized by significant morphological and gene/protein expression changes in prostate cancer tumours compared to static conditions.[7]

In the current study, we developed a computational model for a 3D perfusion bioreactor model and porous scaffolds to replicate the *in vivo* conditions of the interstitial fluid transport in bone. Overall, our numerical and experimental results indicate that our current bioreactor design achieved the *in vivo* conditions. For instance, the flow velocities between the scaffolds and on the scaffold surface (Case B) were observed between 0 and 20 μm/s, which are well within the physiological range of the interstitial flow,[14] were obtained by maintaining a 0.2 mL/min flow rate. The fluid-induced shear stress on the surface of the scaffolds (Case B) was observed to reach a magnitude up to 60 μPa. Our previous work also demonstrated that the proliferation and osteogenic differentiation of hMSCs were enhanced under FSS of approximately 10 μPa.[7] Our results in Fig. 8 showed that FSS in our bioreactor attained the magnitude up to 100 μPa. Note that *in vitro* experiments have shown that significant osteogenic differentiation of hMSCs occurs under FSS range of [10−1000] μPa.[6] Thus, our bioreactor design is able to provide physiological FSS values to promote bone formation.

There is a variation of hydrodynamic conditions and the associated cellular growth among scaffolds as shown in Figs. 5 and 8. First, the cell viability showed the signatures of hMSCs proliferation across all back surfaces of the four scaffolds (Fig. 5b). However, there exist a considerable difference on the cell distribution pattern (blue pixels). To explain this phenomenon, we re-examined the shear stress patterns on each scaffold separately using the large-scale simulation (Case B) in Fig. 8. While FSS diverges toward the edges on the front surface, it converges toward the center on the back surface in the first scaffold. This convergence coincides with the proliferation of cells on the back surface, which is not observed on the front surface (Fig. 2). Moreover, the FSS magnitude is much lower on the back surface (less than 10 μPa) in comparison to the one on the front surface ($\sim$ 60 μPa) as seen in Fig. 8c. This observation suggests that the hMSCs can only proliferate under low shear stress. Indeed, the consecutive placement of the scaffolds created low flow and low shear stress regions between the scaffolds as shown in Figs. 8b and 8c. The FSS magnitude on the second, third, and fourth scaffold did not go beyond 20 μPa. The cells were able to grow on the back surfaces of these scaffolds as shown in Fig. 5. In brief, our work suggests that the magnitude of FSS should be within [10−20] μPa to promote bone growth.

The distribution of FSS has been hypothesized to be dependent on scaffold's pore size and architecture.[19] Therefore, it is critical to resolve the scaffold geometries accurately. However, resolving flow condition in the pores of the full-scale 3D scaffold is a challenging task. The complexity of the porous structures requires a sufficiently fine mesh to accurately capture the pores as shown in Table 1. Past works simplified the computational domain and focused only on sub-domains, which are local regions of the scaffold.[20] In the present study, numerical simulations were performed using the entire scaffold geometry (micro-CT scan) to provide a realistic distribution of FSS within the pores. Our computational data showed strong evidence of correlation between the FSS direction, scaffold porosity and the cells proliferation. Our high-resolution simulation (Case C) in Fig. 9 shows that FSS distribution is heterogeneous on the scaffold surfaces. In particular, the shear stress pattern on the back surface of the scaffold (Fig. 9b) indicates an intricate flow surrounding the pore holes. The FSS was observed to converge around the pores creating a shear dominant direction (Figs. 9c, 9d). Our histological observations in Figs. 6c and 6d indicated a localized growth of cells near the edges of the pores under dynamic condition, where a such localized growth was not observed in the static condition both in the large-scale (Fig. 6a) nor locally near the pores (Fig. 6b). Under the static condition, the patterns of the hMSCs and prostate cancer cells were randomly distributed. Under dynamic condition, the cells grew locally in the vicinity of the pores where the shear stress is high as shown in Fig. 7. The distribution and morphology of prostate cancer cells on Day 23 (+10) and Day 23 (+20) under dynamic condition in Fig. 7 also showed a similar trend. Moreover, the morphological orientation of individual cells in Figs. 5b, 6, and 7 agreed well with the direction of the applied FSS (Figs. 9c, 9d). Based on our experimental and computational studies, we found that FSS significantly altered the distribution, morphology and growth of the co-cultured hMSCs and prostate cancer cell. Therefore, our work suggests that FSS is responsible on regulating the distribution of cells on the pore edges.

Another advantage of this approach is the ability to resolve the flow circulation zone between two consec-

utive scaffolds as illustrated in Fig. 11a. Our results showed that the velocity and shear stress distributions on the first scaffold were minimally affected by the presence of the second scaffold (Figs. 10c, 10d, 11c, 11d). This analysis indicates that the approaching velocity on the scaffold surfaces is mostly in the range of [0.1−5] μm/s which is in the physiological ranges.[14] The fluid-induced shear stress is approximately around [1−10] μPa. Therefore, future experimental works can utilize these ranges in designing three-dimensional tumor models.

Our computational approach is limited by the spatial resolution of the micro-CT images, which is at 70 μm. At this resolution, the cell morphology cannot be captured by the micro-CT scan. Consequently, the impact of the cell morphology on the flow velocities and shear stresses is not considered in our computation model.

Conclusion

Our computational and experimental results in a 3D perfusion bioreactor demonstrate the impacts of fluid shear stress (FSS) on the growth of co-cultured hMSCs and MDAPCa2b cells. Our results indicate that the cellular viability is favored under a specific range of hydrodynamics, which are at [0.1−5] μm/s (flow velocity) and [1−10] μPa (shear stress), respectively. The cell proliferation is enhanced significantly at the boundaries of the scaffold pores, which are the convergent lines of the local FSS vectors. Our simulation results suggest that the stretching of the hMSCs correlates to the local direction of the FSS. Future works are needed to quantify this correlation in details.

ACKNOWLEDGMENTS

This work is supported by the NSF Grant Number 1946202 (ND-ACES) and a start-up package of Trung Le from North Dakota State University. The authors acknowledge the use of computational resources at the Center for Computationally Assisted Science and Technology (CCAST)-NDSU, which is supported by the NSF MRI 2019077. The authors also received an allocation (CTS200012) from the Extreme Science and Engineering Discovery Environment (XSEDE). We acknowledge the financial support of NIH-2P20GM103442-19A1 to train undergraduate students in Biomedical Engineering.

CONFLICT OF INTEREST

The authors have no conflicts of interest to declare.

REFERENCES

[1]Akerkouch, L., and T. B. Le. A hybrid continuum-particle approach for fluid-structure interaction simulation of red blood cells in fluid flows. *Fluids*, 6(4):139, 2021.

[2]Ambre, A. H., S. Payne, K. S. Katti, and D. R. Katti. Vesicular delivery of crystalline calcium minerals to ecm in biomineralized nanoclay composites. *Mater. Res. Express*, 2(4):045401, 2015.

[3]Bancroft, G. N., V. I. Sikavitsas, J. V. D. Dolder, T. L. Sheffield, C. G. Ambrose, J. A. Jansen, and A. G. Mikos. Fluid flow increases mineralized matrix deposition in 3d perfusion culture of marrow stromal osteoblasts in a dose-dependent manner. *PNAS*, 99(20):12600–12605, 2002.

[4]Buchanan, C. F., S. S. Verbridge, P. P. Vlachos, and M. N. Rylander. Flow shear stress regulates endothelial barrier function and expression of angiogenic factors in a 3d microfluidic tumor vascular model. *Cell Adhes. Migr.*, 8(5):517–24, 2014.

[5]Cartmell, S. H., B. D. Porter, A. J. Garcia, and R. E. Guldberg. Effects of medium perfusion rate on cell-seeded three-dimensional bone constructs in vitro. *Tissue Eng.*, 9:1197–1203, 2003.

[6]Gao, X., X. Zhang, H. Xu, B. Zhou, W. Wen, and J. Qin. Regulation of cell migration and osteogenic differentiation in mesenchymal stem cells under extremely low fluidic shear stress. *Biomicrofluidics*, 8:052008, 2014.

[7]Jasuja, H., S. Kar, D. R. Katti, and K. S. Katti. Perfusion bioreactor enabled fluid-derived shear stress conditions for novel bone metastatic prostate cancer testbed. *Biofabrication*, 13:035004, 2021.

[8]Katti, D. R., A. H. Ambre, and K. S. Katti. Biomineralized hydroxyapatite nanoclay composite scaffolds with polycaprolactone for stem cell-based bone tissue engineering. *J. Biomed. Mater. Res. A*, 103(6):2077–101, 2015.

[9]Katti, D. R., J. Iswara, R. Venkatesan, R. Paulmurugan, M. D. S. Molla, and K. S. Katti. Prostate cancer phenotype influences bone mineralization at metastasis: a study using an in vitro prostate cancer metastasis testbed. *JBMR Plus*, 4(2):e10256, 2020.

[10]Katti, D. R., K. Kundu, S. V. Jaswandkar, and K. S. Katti. Initial upsurge of bmps enhances long-term osteogenesis in in-vitro bone regeneration. *Materialia*, 26(12):101576, 2022.

[11]Le, T. B., D. R. Troolin, D. Amatya, E. K. Longmire, and F. Sotiropoulos. Vortex phenomena in sidewall aneurysm hemodynamics: experiment and numerical simulation. *Ann. Biomed. Eng.*, 41(10):2157–2170, 2013.

[12]Molla, M. D. S., F. Karandish, M. K. Haldar, S. Mallik, K. S. Katti, D. R. Katti. Sequential culture on biomimetic nanoclay scaffolds forms three-dimensional tumoroids. *J. Biomed. Mater. Res.*, 104(7):1591–1602, 2016.

[13]Molla, M. D. S., D. R. Katti, and K. S. Katti. In vitro design of mesenchymal to epithelial transition of prostate cancer metastasis using 3d nanoclay bone-mimetic scaffolds. *J. Tissue Eng. Regen. Med.*, 12(3):727–737, 2018.

[14]Nava, M. M., K. Yeager, A. Chramiec, L. Hao, S. Robinson, E. Guo, M. T. Raimondi, A. Marturano-Kruik, and G. Vunjak-Novakovic. Human bone perivascular niche-on-a-chip for studying metastatic colonization. *Cell Rep.*, 115(6):1256–1261, 2018.

[15]Polacheck, W. J., J. L. Charest, and R. D. Kamm. Interstitial flow influences direction of tumor cell migration through competing mechanisms. *Proc. Natl. Acad. Sci.*, 108(27):11115–11120, 2011.

[16]Roodman, G.D. Mechanisms of bone metastasis. *N. Engl. J. Med.*, 350(16):1655–1664, 2004.
[17]Shah, A.D., M.,J. Bouchard, and A. C. Shieh. Interstitial fluid flow increases hepatocellular carcinoma cell invasion through cxcr4/cxcl12 and mek/erk signaling. *PLoS ONE*, 10(11):e0142337, 2015.
[18]Yourek, G., S. M. McCormick, J. J. Mao, and G. C Reilly. Shear stress induces osteogenic differentiation of human mesenchymal stem cells. *Regen. Med.*, 5(5):713, 2010.
[19]Zermatten, E., J. R. Vetsch, D. Ruffoni, S. Hofmann, R. Muller, and A. Steinfeld. Micro-computed tomography based computational fluid dynamics for the determination of shear stresses in scaffolds within a perfusion bioreactor. *Ann. Biomed. Eng.*, 42(5):1085–1094, 2014.
[20]Zhao, F., J. Melke, K. Ito, B. V. Rietbergen, and S. Hofmann. A multiscale computational fluid dynamics approach to simulate the micro-fuidic environment within a tissue engineering scafold with highly irregular pore geometry. *Biomech. Model Mechanobiol.*, 18(6):1965–1977, 2019.